Spray Coating Experiments: Setups and Methodologies

The latest eBook from Advanced Optical Metrology. Download for free.

Spray Coating Experiments: Setups and Methodologies, is the third in our Thin Films eBook series. This publication provides an introduction to spray coating, three article digests from Wiley Online Library and the latest news about Evident's Image of the Year Award 2022.

Wiley in collaboration with Evident, are committed to bridging the gap between fundamental research and industrial applications in the field of optical metrology. We strive to do this by collecting and organizing existing information, making it more accessible and useful for researchers and practitioners alike.

EVIDENT
OLYMPUS

WILEY

NANO · MICRO small
www.small-journal.com

Toward the High-Performance Lithium Primary Batteries by Chemically Modified Fluorinate Carbon with δ-MnO_2

Luyu Li, Ruizhe Wu, Hancheng Ma, Bingbing Cheng, Shaoqing Rao, Sheng Lin, Chunbo Xu, Lei Li, Yao Ding, and Liqiang Mai**

Li/CF_x battery is one of the most promising lithium primary batteries (LPBs) which yields the highest energy density but with poor rate capability. This Achilles'' heel hinders the large-scale applications of Li/CF_x batteries. This work first reports a facile chemical modification method of CF_x with δ-MnO_2. Having benefited from the chemical bonding, the electrochemical performance at high-rate discharge is remarkably enhanced without compromising the specific capacity. The coin cells exhibit an energy density of 1.94×10^3 Wh kg^{-1} at 0.2 C, which is approaching the theoretical energy density of commercial fluorinated graphite (2.07×10^3 Wh kg^{-1}). A power density of 5.49×10^4 W kg^{-1} at 40 C associated with an energy density of 4.39×10^2 Wh kg^{-1}, which is among the highest value of Li/CF_x batteries, are obtained. Besides, the punch batteries achieve an ultrahigh power density of 4.39×10^4 W kg^{-1} with an energy density of 7.60×10^2 Wh kg^{-1} at 30 C. The intrinsic reasons for this outstanding electrochemical performance, which are known as the fast Li^+ diffusion kinetics guided by thin δ-MnO_2 flakes and the low formation energy barrier caused by chemical bonding, are explored by the galvanostatic intermittent titration technique (GITT) and theoretical calculations.

1. Introduction

Lithium primary batteries (LPBs), refer to the non-rechargeable primary batteries with lithium metal as the anode,[1,2] have possessed an important role in the applications for critical environment, for example, deep underground or in tire-pressure monitoring systems.[3] Among the LPBs, lithium fluorinated carbon batteries (Li/CF_x) have a wide range of applications in civilian, military and other fields due to their high theoretical energy density (2180 Wh kg^{-1}), high theoretical specific capacity (865 mAh g^{-1}), stable working voltage (open circuit voltage as 3.0–3.2 V), wide operating temperature range (–40 to 80 °C) and excellent environmental stability (more than 10 years).[4–6] However, when discharged at the high rate, due to the intrinsic low electronic conductivity,[7–9] these Li/CF_x batteries always suffer from poor kinetics and cause a serious voltage delay. Therefore, the capacity and voltage platform will be significantly reduced, which greatly limits the application and promotion of Li/CF_x batteries.

In order to solve these problems, considerable efforts have been devoted in recent years, such as chemical modification (e.g., N doping)[10] and optimization of the composition of cathodes.[11] One mainstream approach is using different carbon materials such as F-HNG[10] and FGS-1.03[12] to control the fluorination process and construct a 3D or porous structure with sufficient channels for Li^+ diffusion. For example, Feng et al. recently reported Li/CF_x batteries with the power density of 7.32×10^4 W kg^{-1} (50 C) by defective N-doped fluorinated carbon.[10] Nevertheless, the reported approaches by creating highly porous or defective 3D carbon structure are cumbersome and difficult to scale up. Moreover, equipment with corrosion resistance is highly demanded due to the fluorination process at high temperature. Surface modification of CF_x with conductive materials is another effective strategy. Generally, researchers usually applied methods of "adding to the material" in order to improve the electrochemical performance of Li/CF_x batteries, such as polypyrrole[9] and carbon coating[13,14] to improve the electrical conductivity, or reaction with H_2,[15] NaOH[3] and SiO_2[11] by removing the inert C—F components to

L. Li, H. Ma, S. Rao, S. Lin, Y. Ding, L. Mai
School of Materials Science and Engineering
Wuhan University of Technology
Wuhan 430070, P. R. China
E-mail: ydingaf@whut.edu.cn; mlq518@whut.edu.cn
R. Wu
Collaborative Innovation Center for Advanced Organic Chemical Materials Co-constructed by the Province and Ministry
Ministry of Education Key Laboratory for the Synthesis and Application of Organic Functional Molecules
College of Chemistry and Chemical Engineering
Hubei University
Wuhan 430062, P. R. China
B. Cheng, C. Xu, L. Li
Wuhan Institute of Marine Electric Propulsion
Wuhan 430064, P. R. China
L. Mai
Hainan Institute
Wuhan University of Technology
Sanya 572000, P. R. China
The ORCID identification number(s) for the author(s) of this article can be found under https://doi.org/10.1002/smll.202300762.

DOI: 10.1002/smll.202300762

facilitate ion transport. However, the improvements of performance are limited and capacity loss is inevitable.

Besides, among the previous researches, another useful method is to integrate CF_x with MnO_2 to prepare hybrid cathodes, in which the MnO_2 components can deliver a higher discharge voltage and improve the voltage hysteresis of the Li/CF_x batteries. In this case, the performance of cells is strongly correlated with the distribution of MnO_2 components. For instance, Feng et al. systematically studied the effects of four CF_x/MnO_2 arrangements (including $CF_x//MnO_2$, CF_x@MnO_2, $CF_x \bigoplus MnO_2$, $MnO_2 \bigoplus CF_x$) on the electrochemical performance, among which the parallel type ($CF_x//MnO_2$) was the best.[16] In addition, Luo[17] et al. synthesized CF_x@MnO_2-nanowires composites by hydrothermal reaction. According to the report, OP-10 emulsifier was first added to disperse the CF_x in water in order to obtain the uniformly dispersed MnO_2 nanowires on surface and results in a better rate capability. Despite all these reports, it is essentially difficult to achieve the uniform and compact hybridization of CF_x/MnO_2 composites due to the lack of chemical interaction at the interface, which is detrimental to the charge and mass transfer during discharge. Consequently, the improvement of rate capability is quite limited with a compromise of the specific energy density.

In this work, we introduce oxygen functional groups in the CF_x structure with acid treatment and then successfully prepare chemically modified δ-MnO_2@CF_x composites by a facile hydrothermal reaction for the first time. The compact and uniform coating of δ-MnO_2 on CF_x surface greatly enhanced the electrochemical performance at high-rate discharge without compromising the specific capacity. Specially, the coin cells exhibit a maximum energy density of 1.94×10^3 Wh kg^{-1} at 0.2 C, which is approaching the theoretical energy density of commercial fluorinated graphite (2.07×10^3 Wh kg^{-1}). More impressively, for the high-rate discharge, it is able to deliver a power density of 5.49×10^4 W kg^{-1} at 40 C associated with an energy density of 4.39×10^2 Wh kg^{-1}, which is among the highest value for previously reported CF_x based cathodes. Besides, the punch batteries also achieve an ultrahigh power density of 4.39×10^4 W kg^{-1} with an energy density of 7.60×10^2 Wh kg^{-1} at 30 C. The outstanding electrochemical performance, especially the rate capability, is significantly improved compared to those of the state-of-the-art. Further theoretical calculations illustrate that the high-performance can be attributed to two key points: first, the active sites (e.g., −OH or −COOH groups) introduced by the acid treatment of CF_x significantly improve the distribution of δ-MnO_2 and help to an ordered transportation channel of Li^+ which accelerate the reaction kinetics. Second, the layered δ-MnO_2 on surface can improve the capacity of Li^+ storage and result in a high energy density. This work outlines a possible approach to obtain the high-performance CF_x based cathodes with low cost and also expands the range of industrial applications of Li/CF_x LPBs.

2. Results and Discussion

For a typical synthesis process (**Figure 1**a) of δ-MnO_2 coated fluorinated carbon (δ-MnO_2@CF_x), in order to introduce the active sites (e.g., carboxyl, hydroxyl groups) for chemical bonding of δ-MnO_2, as well as improving the hydrophilicity of CF_x, CF_x (x = 0.6) powder should be first treated by concentrated H_2SO_4/HNO_3 (volume ratio 3:1) to prepare O−CF_x. High-resolution X-ray photoelectron spectroscopy (XPS) characterization is used to analyze the chemical states of C in O−CF_x and CF_x. As shown in Figure 1b, comparing the C 1s spectrum of CF_x with that of O−CF_x, the C 1s spectrum can be fitted into five different states of carbon species at a binding energy as 284.8 eV for C−C, 286.4 eV for C−O, 290.1 eV for C−F, 292.0 eV for C−F_2 and 292.6 eV for C−F_3, while the C 1s spectrum of O−CF_x is fitted to five different states of carbon species at a bonding energy of 284.8 eV for C−C, 286.1 eV for C−O, 287.8 eV for C=O, 290.1 eV for C−F and 292.0 eV for C−F_2.[18,19] By comparison, the intensity of C−C decreases, while the C=O peak at 287.8 eV appears and the intensity of C−O at 286.3 eV increases for O−CF_x, which demonstrates the successful attachment of O onto the CF_x structure. On the other hand, there is no obvious change for the C−F or C−F_2 signal, and the F atomic ratio is 36.31% and 32.17% in pristine and treated CF_x, respectively. Therefore, the C−F bonds are preserved during the oxidation reaction, which is important to maintain the discharge capacity of the material. Therefore, with the introduction of oxygen-containing functional groups, O−CF_x can be well dispersed in water and hydrothermal reaction is conducted with the addition of $KMnO_4$ to synthesize δ-MnO_2@CF_x. After the acid treatment, O−CF_x and $KMnO_4$ are dispersed in DI water to synthesis the δ-MnO_2@CF_x by the hydrothermal reaction. The MnO_4^- groups disperse onto the surface of O−CF_x and interact with the active sites, thereby which achieves a precise chemical bonding on the surface with fluorinated carbon. By controlling the reaction time (3 and 6 h in this work), the thickness of δ-MnO_2 layers can be adjusted.

After synthesis, the structure of δ-MnO_2@CF_x is characterized by X-ray diffraction (XRD) and Raman spectroscopy. Figure 1c shows the XRD spectra of CF_x, pure δ-MnO_2 and δ-MnO_2@CF_x composites synthesized by 3 and 6 h hydrothermal reaction (δ-MnO_2@CF_x-3 h and δ-MnO_2@CF_x-6 h, respectively). For CF_x, two peaks located at around 2θ = 12.5° and 41° can be attributed to the diffraction of (001) and (100) lattice planes of fluorinated carbon in Figure S1, Supporting Information, which can be observed in three samples (CF_x, δ-MnO_2@CF_x-3 h, and δ-MnO_2@CF_x-6 h). The peak at 2θ = 27.5° can be assigned to the (002) reflection peak because of poor regularity along the stacking direction,[20] which can also be observed in three samples (CF_x, δ-MnO_2@CF_x-3 h, and δ-MnO_2@CF_x-6 h). Besides, δ-MnO_2 flowers, which consist of 2D edge-shared MnO_6 octahedral layers with K^+ cations and water molecules in the interlayer space,[21] are synthesized by hydrothermal reaction (see Experimental Section for details). The full XRD patterns of this δ-MnO_2 (Figure S1, Supporting Information) can be well indexed to the monoclinic potassium birnessite (JCPDS #42-1317), in which four representative diffraction peaks at 2θ = 12.5°, 25°, 36.7° and 65.6° correspond to the (001), (002), (11–1) and (31–2) planes, respectively.[22] Besides, these peaks can be also observed in both δ-MnO_2@CF_x-3 h and δ-MnO_2@CF_x-6 h samples verifying the high crystallinity of the composites. Figure 1d presents the Raman spectra of the four samples. For pristine CF_x, two major peaks are detected at about 1315 (D band) and 1573 cm^{-1} (G band). For δ-MnO_2, the peak located

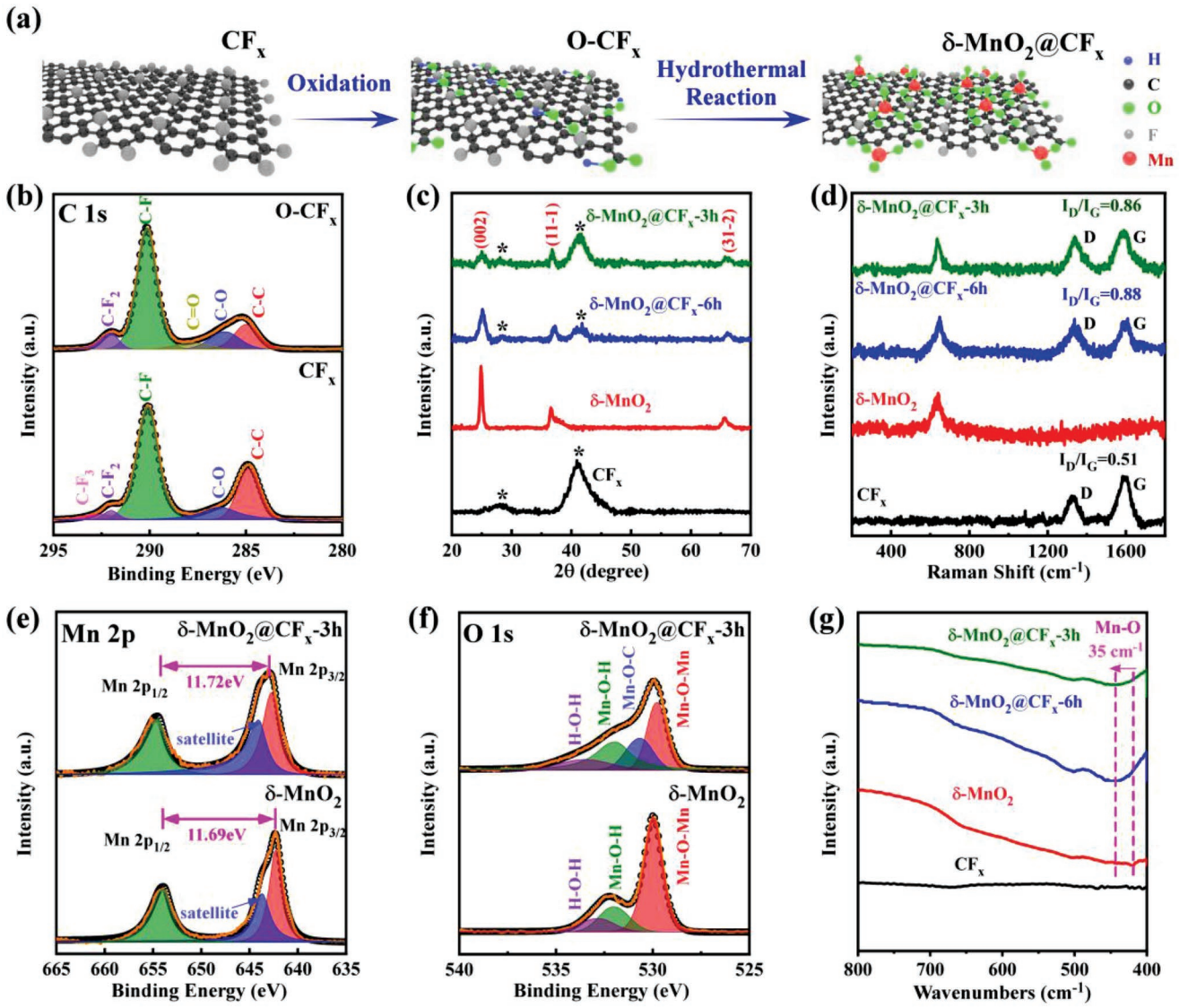

Figure 1. Synthesis and characterization of δ-MnO_2@CF_x. a) Schematic illustration of the fabrication procedure of δ-MnO_2@CF_x. b) C 1s XPS spectra of the CF_x and O—CF_x. c) Ex situ XRD patterns. d) Raman patterns of four samples. e) Mn 2p XPS spectra of the δ-MnO_2@CF_x-3 h and δ-MnO_2. f) O 1s XPS spectra of the δ-MnO_2@CF_x-3 h and δ-MnO_2. g) Fourier transform infrared (FT-IR) patterns of four samples.

at 630 cm^{-1} is assigned to δ-MnO_2,[22,23] which can also be observed in both δ-MnO_2@CF_x composites, further confirming the existence of δ-MnO_2 in the composites. The band located at 630 cm^{-1} can be attributed to the symmetric stretching vibration Mn—O of MnO_6 groups along the interlayer direction. The frequency of this Mn—O stretching mode at high wavenumber can shift as a function of the interlayer spacing of birnessite, which is related to local lattice distortion.[24] In addition, since the ratio of the D band and G band intensity (I_D/I_G) is used to evaluate the disorder in the graphitic materials,[25] the higher I_D/I_G value of δ-MnO_2@CF_x-3 h (I_D/I_G = 0.86) and δ-MnO_2@CF_x-6 h (I_D/I_G = 0.88) compared to the pristine CF_x (I_D/I_G = 0.51) suggests the formation of more defects in the fluorinated carbon structure during the synthesis process.

To further analyze the chemical interaction between δ-MnO_2 and CF_x in the composites, high-resolution XPS is conducted. Figure 1e shows the Mn 2p XPS spectra of δ-MnO_2 and δ-MnO_2@CF_x-3 h, both of which display doublet peaks of Mn $2p_{3/2}$ at 642.2 eV and Mn $2p_{1/2}$ at 653.9 eV. The spin energy difference between two peaks is 11.7 eV, which is the characteristic of MnO_2.[26,27] More importantly, as shown in Figure 1f, the O 1s spectrum of δ-MnO_2 can be fitted by three different states of oxygen species at the binding energy of 530.0 eV for Mn—O—Mn, 532.0 eV for Mn—O—H and 532.8 eV for H—O—H, while that of δ-MnO_2@CF_x-3 h can be deconvolved into four separate peaks centered at 529.8 eV for Mn—O—Mn, 530.6 eV for Mn—O-C, 531.9 eV for Mn—O—H and 533.5 eV for H—O—H.[28] The appearance of the C—O—Mn peak in δ-MnO_2@CF_x-3 h proved the formation of chemical bonds between δ-MnO_2 and CF_x,[29] which is different from those previously reported physically mixed MnO_2/CF_x hybrids.[16,17,30] The chemical structure of δ-MnO_2@CF_x composites are further

studied through Fourier transform infrared (FT-IR) spectroscopy characterization. As shown in Figure 1g and Figure S2, Supporting Information, the absorption bands located at 1220 and 1330 cm^{-1} in both CF_x and δ-MnO_2@CF_x composites are attributed to the C—F bonds and C—F_2 bonds, respectively.[31] It is worth noting that the Mn—O bonds of the δ-MnO_2@CF_x show a blue shift from about 421 to 456 cm^{-1} compared with that of δ-MnO_2, which is due to the formation of C—O—Mn bonds between δ-MnO_2 and CF_x.[32] Also, the intensity of Mn—O bonds in δ-MnO_2@CF_x-6 h is stronger than that in the δ-MnO_2@CF_x-3 h, which further accounts for the less loading of δ-MnO_2 in δ-MnO_2@CF_x-3 h. These results are in good agreement with the above XPS characterizations demonstrating the chemical bonding characteristic between δ-MnO_2 and CF_x.

The morphologies of δ-MnO_2@CF_x-3 h and δ-MnO_2@CF_x-6 h are characterized by scanning electron microscope (SEM) and TEM as shown in **Figure 2**. Figures 2b,c,j,k show the TEM images of δ-MnO_2@CF_x-3 h and δ-MnO_2@CF_x-6 h at low and high magnification, respectively. It can be observed that MnO_2 flakes are uniformly distributed on the surface of CF_x in both δ-MnO_2@CF_x-3 h and δ-MnO_2@CF_x-6 h composites, and the longer synthesis time can produce denser MnO_2 flakes as shown in Figures 2a and 2i. The corresponding TEM image in Figure 2b,j illustrated that the MnO_2 stuck tightly to the CF_x surface. The crystallinity of the δ-MnO_2 in both composites are verified by high-resolution transmission electron microscopy (HRTEM) images in Figures 2c and 2k, the (001) layer spacing of MnO_2 flakes has been measured to be 0.6 and

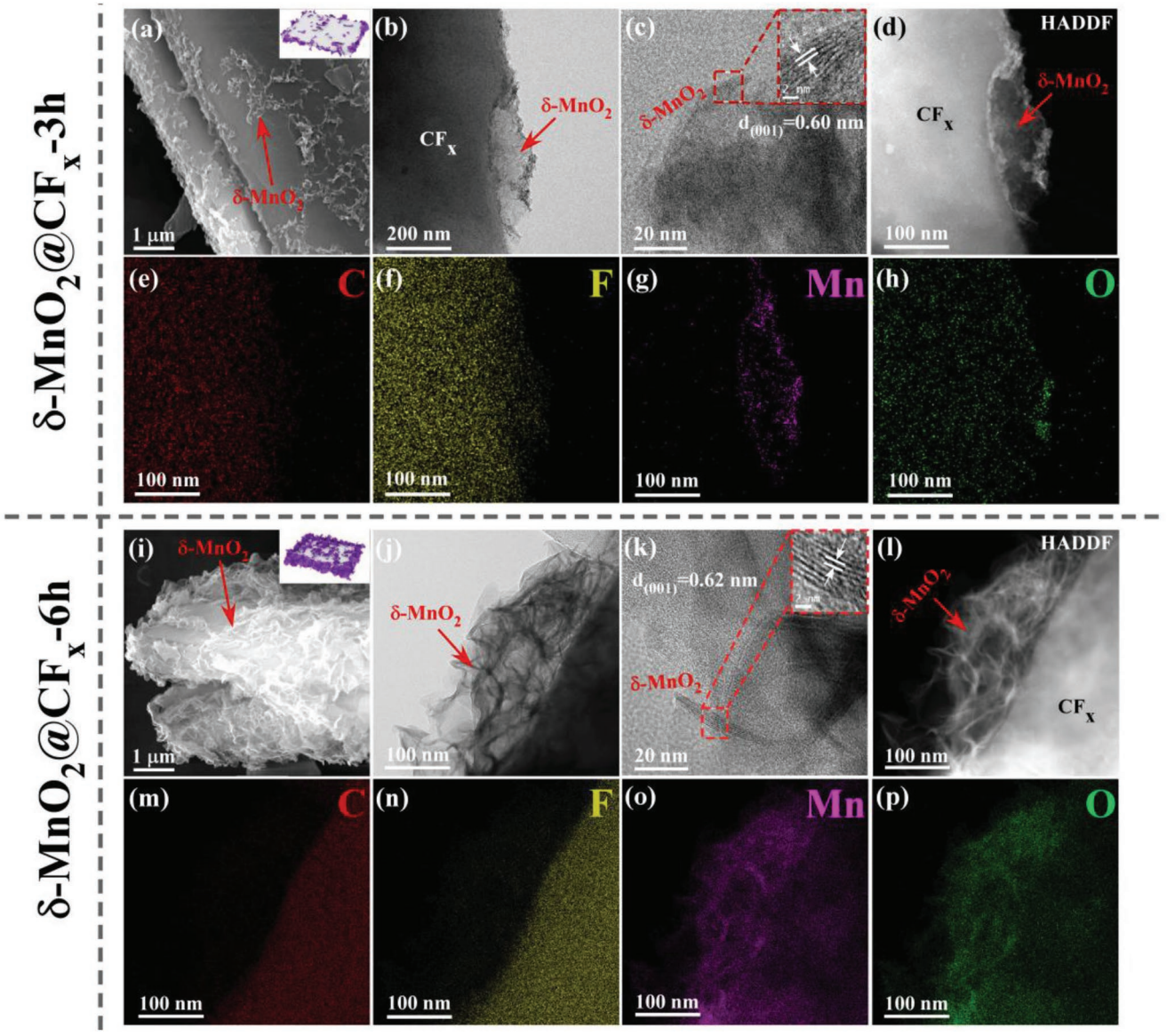

Figure 2. SEM and TEM images of δ-MnO_2@CF_x with 3 h (δ-MnO_2@CF_x-3 h) and 6 h (δ-MnO_2@CF_x-6 h) synthesis. a,i) SEM images of δ-MnO_2@CF_x-3 h and δ-MnO_2@CF_x-6 h. Inset: schematic of the structure of δ-MnO_2@CF_x-3 h and δ-MnO_2@CF_x-6 h. b,j) TEM images of δ-MnO_2@CF_x-3 h and δ-MnO_2@CF_x-6 h. c,k) HRTEM images of δ-MnO_2@CF_x-3 h and δ-MnO_2@CF_x-6 h. Inset: layer spacing of related materials. d,l) HADDF images of δ-MnO_2@CF_x-3 h and δ-MnO_2@CF_x-6 h. e–h,m–p) TEM-EDX mapping images of δ-MnO_2@CF_x-3 h and δ-MnO_2@CF_x-6 h.

0.62 nm for δ-MnO_2@CF_x-3 h and δ-MnO_2@CF_x-6 h, respectively, which is in good agreement with the birnessite-type MnO_2.[33] Figure 2e–h presents the energy dispersive X-ray spectroscopy (EDX) elemental mapping of the δ-MnO_2@CF_x-3 h, from which the coated δ-MnO_2 can be viewed in an intuitive way. The elemental distribution of F in δ-MnO_2@CF_x-3 h can also be slightly detected. On the one hand, the size of F is smaller than the layer spacing of δ-MnO_2. There is probably some F existed in the interlayer of δ-MnO_2 like K^+.[34] It's also possible that the F signals come from the thin CF_x flakes below, as weak C signals at the same place can be observed in Figure 2e. Besides, the mapping results (Figure 2m–p) of δ-MnO_2@CF_x-6 h in Figure 2l illustrated similar elemental distribution characteristics, while the intensity of Mn and O elements on the surface are stronger indicating the thicker layers of MnO_2 with 6 h synthesis.

In order to compare the electrochemical performance of pristine CF_x, pure δ-MnO_2, physically mixed δ-MnO_2/CF_x and chemically modified δ-MnO_2@CF_x at different discharge rates, the galvanostatic discharge curves (GDC) of four cathodes are presented in **Figure 3**. The discharge current at different rates is calculated by the theoretical values (CF_x: 865 mAh g^{-1}; MnO_2: 308 mAh g^{-1}; δ-MnO_2@CF_x-3h: 809 mAh g^{-1} based on the mass percentage of δ-MnO_2 as 10 wt%; δ-MnO_2@CF_x-6h: 753 mAh g^{-1} based on the mass percentage of δ-MnO_2 as 20 wt%. The mass percentage is confirmed by inductive coupled plasma emission spectrometer (ICP) test as shown in Figure S4, Supporting Information. The commercial CF_x exhibits a specific capacity of 780 mAh g^{-1} at 0.2 C, while the specific capacity dramatically reduces to 423 mAh g^{-1} when discharged at a high rate of 10 C (Figure 3a). In addition, an obvious voltage delay can be observed indicating the poor rate capability of pristine CF_x. On the other hand, δ-MnO_2 represents a relatively low specific capacity of 85.1 mAh g^{-1} at 0.2 C, but without obvious voltage delay at 10 C discharge rate (Figure 3b). The specific capacity is much smaller than the reported value of ≈200 mAh g^{-1},[16] because the δ-MnO_2 has not been dehydrated by thermal treatment (usually between 250 and 400 °C) after hydrothermal reaction, which can remove problematic water content and create a structure more suitable for lithium intercalation.[35] Therefore, many previous reports have applied MnO_2/CF_x hybrids to achieve rate capability and high capacity at the same time.[16,17,30] Here, in order to compare the electrochemical performance of chemically modified δ-MnO_2@CF_x with those hybrid cathodes by physical mixing, we also fabricated physically mixed MnO_2/CF_x cathodes, that is, δ-MnO_2/CF_x(1:9) and δ-MnO_2/CF_x(1:4) with MnO_2 mass ratio same as δ-MnO_2@CF_x-3 h and δ-MnO_2@CF_x-6 h, respectively. As shown in Figures 3c and 3d, the specific capacities of δ-MnO_2/CF_x(1:4) and δ-MnO_2/CF_x(1:9) are 686 and 735.3 mAh g^{-1} at 0.2 C, respectively. Here, the specific capacity of δ-MnO_2/CF_x(1:4) is lower because δ-MnO_2 accounts for a greater proportion as was expected. In addition, the rate capability of the δ-MnO_2/CF_x(1:9) and δ-MnO_2/CF_x(1:4) hybrids is improved as the discharge plateau is higher and there is no obvious voltage delay even at 10 C discharge rate. For example, the discharge plateau of δ-MnO_2/CF_x(1:9) and δ-MnO_2/CF_x(1:4) at 2 C is 2.26 and 2.32 V (versus Li^+/Li), respectively, which is higher than that of pristine CF_x (2.16 V versus Li^+/Li), while the discharge capacity of both is lower than that of pristine CF_x. It is even more evident when discharged at 5 C that the δ-MnO_2/CF_x(1:4) with a larger MnO_2 proportion exhibits a significantly higher voltage plateau at 2.12 V compared with that of pristine CF_x and δ-MnO_2/CF_x(1:9) (<2 V). Unfortunately, the corresponding specific capacity of δ-MnO_2/CF_x(1:4) and δ-MnO_2/CF_x(1:9) is only 370.5 and 385.5 mAh g^{-1}, respectively. Therefore, the physically mixed δ-MnO_2/CF_x cathodes represent a relatively good rate capability but a poor specific capacity due to the amount of δ-MnO_2 is positively correlated with the discharge plateau but negatively correlated with the specific capacity.

More importantly, the GDCs of chemically modified δ-MnO_2@CF_x cathodes (δ-MnO_2@CF_x-6 h and δ-MnO_2@CF_x-3 h) at different current densities are shown in Figures 3e and 3f. The specific capacity of δ-MnO_2@CF_x-3 h is 804.2 mAh g^{-1} at 0.2 C, which is close to the pristine CF_x, while the value of δ-MnO_2@CF_x-6 h is 695.6 mAh g^{-1}. When discharged at 2 C, the voltage plateau of δ-MnO_2@CF_x-6 h and δ-MnO_2@CF_x-3 h is 2.25 V similar to the above physically mixed samples. However, the discharge capacity of δ-MnO_2@CF_x-6 h and δ-MnO_2@CF_x-3 h is distinguished higher at 590.3 and 766.4 mAh g^{-1}, respectively. When the discharge current density increases to 5 C, the δ-MnO_2@CF_x-3 h outperforms the above samples with a voltage plateau at 2.12 V and a capacity of 696.4 mAh g^{-1}. Even at the ultrafast discharge rate of 30 C, a significantly high capacity of 409.6 mAh g^{-1} can still be obtained for the δ-MnO_2@CF_x-3 h. Furthermore, the specific capacity of δ-MnO_2@CF_x-3 h is 260.6 mAh g^{-1} at 40 C. It is suggested that the better rate capability of the δ-MnO_2@CF_x-3 h than the δ-MnO_2@CF_x-6 h results from the thinner MnO_2 shell which has less side effect on Li^+ diffusion into the CF_x. And the rate capability of δ-MnO_2@CF_x-3 h is also better than that of the δ-MnO_2@CF_x-2 h and δ-MnO_2@CF_x-4 h (Figure S5, Supporting Information).

The histograms in Figures 3g and 3h present the variation of both energy and power densities for CF_x, δ-MnO_2/CF_x(1:9), and δ-MnO_2@CF_x-3 h cathodes calculated by their GDCs at different rates. δ-MnO_2@CF_x-3 h cathodes exhibit a maximum energy density of 1.94×10^3 Wh kg^{-1} at 0.2 C, which is approaching the theoretical energy density of commercial fluorinated graphite (2.07×10^3 Wh kg^{-1}). Moreover, when discharged at 10 C, the δ-MnO_2@CF_x-3 h cathodes still exhibited a superior energy density of 1.34×10^3 Wh kg^{-1} in comparison with that of CF_x (7.40×10^2 Wh kg^{-1}) and δ-MnO_2/CF_x(1:9) (5.21×10^2 Wh kg^{-1}). It is even more impressive that δ-MnO_2@CF_x-3 h is able to deliver a maximum power density of 5.49×10^4 W kg^{-1} at 40 C associated with an energy density of 4.39×10^2 Wh kg^{-1}, which is one of the best performances for CF_x based cathodes compared with previous works (**Table 1**). The electrochemical performance of chemically modified δ-MnO_2@CF_x is much better than that of pristine CF_x and physically mixed δ-MnO_2/CF_x hybrids in both energy density and power density at all discharge rates, which is important to expand the range of applications.

The kinetics of the electrochemical reaction in CF_x, δ-MnO_2/CF_x, and δ-MnO_2@CF_x cathodes is further compared by electrochemical impedance spectroscopy (EIS) as shown in **Figure 4**a,b. In the equivalent circuit model, R_b, R_{ct}, Z_w and C_d denote ohmic resistance, charge-transfer resistance, Warburg

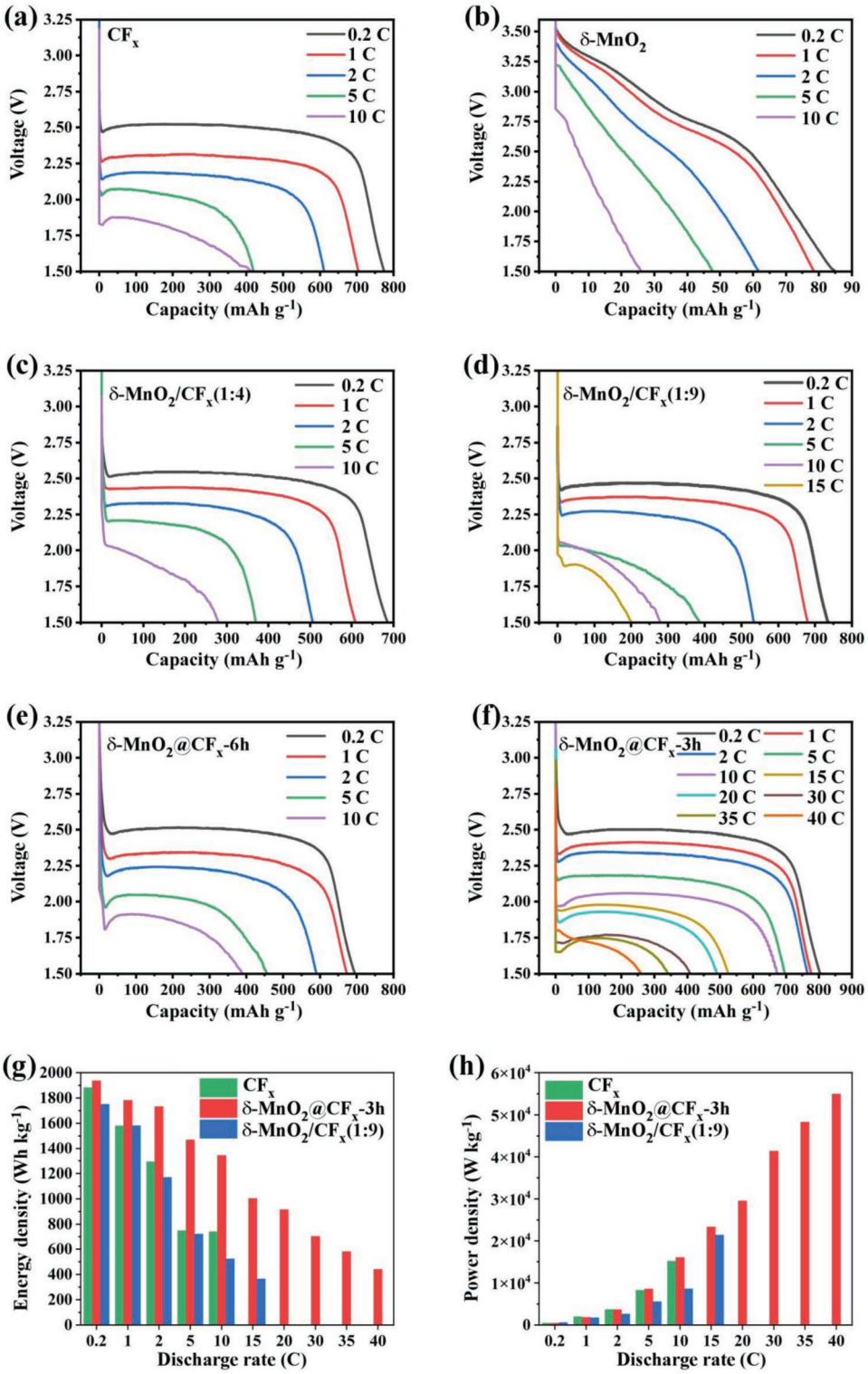

Figure 3. Electrochemical performance of δ-MnO_2@CF_x. a–f) The galvanostatic discharge curve of a) CF_x, b) δ-MnO_2, c) δ-MnO_2/CF_x(1:4), d) δ-MnO_2/CF_x(1:9), e) δ-MnO_2@CF_x-6 h, and f) δ-MnO_2@CF_x-3 h at different discharge rates. g) Energy density of δ-MnO_2@CF_x-3 h compared with CF_x and δ-MnO_2/CF_x(1:9) cathodes. h) Power density of δ-MnO_2@CF_x-3 h compared with CF_x and δ-MnO_2/CF_x(1:9) cathodes.

impedance and double-layer capacitance, respectively.[12,36] The combination of the electrode, separator, electrolyte and collector results in R_b resistance.[37] The R_{ct} corresponds to the semicircle in the impedance plot and the Warburg impedance Z_w related to the diffusion of Li^+ in the CF_x, δ-MnO_2/CF_x, and δ-MnO_2@CF_x electrodes which is indicated by a straight sloping line at

Table 1. Comparison of the electrochemical performance of δ-MnO_2@CF_x-3 h cathodes in this study and previously reported CF_x based cathodes.

Samples	Maximum discharge rate [C]	Capacity [mAh g^{-1}]	Discharge plateau [V]	Power density [W kg^{-1}]
δ-MnO_2@CF_x-3 h (this work)	40	260.6	1.71	5.49×10^4
CF_x//MnO_2[16]	5	323.4	1.73	6.16×10^3
CF_x-$mSiO_2$[11]	5	587	2.28	9.69×10^3
GACP based $CF_{1.0}$[42]	5	653	2.01	8.0×10^3
Surface de-fluorination[3]	30	500	1.86	4.84×10^4
Gaseous electrolyte additive BF_3[43]	15	415.5	1.74	2.30×10^4
H-CF_x[15]	10	402	2.19	$\approx 1.50 \times 10^4$
FGS-1.03[12]	50	504.7	1.63	7.12×10^4
F-HNG-200[10]	50	≈350	1.80	7.32×10^4

low frequencies.[16] δ-MnO_2@CF_x presents the much smaller R_{ct} and Z_w values than CF_x and δ-MnO_2/CF_x, demonstrating a faster diffusion kinetic of Li^+. Furthermore, δ-MnO_2@CF_x-3 h cathodes have the lowest R_{ct} value, which implies the fastest diffusion among all samples due to the chemical bonding and a thinner δ-MnO_2 coating, consistent with the above results of discharge. Therefore, the importance of the chemical modification in δ-MnO_2@CF_x is strengthen.

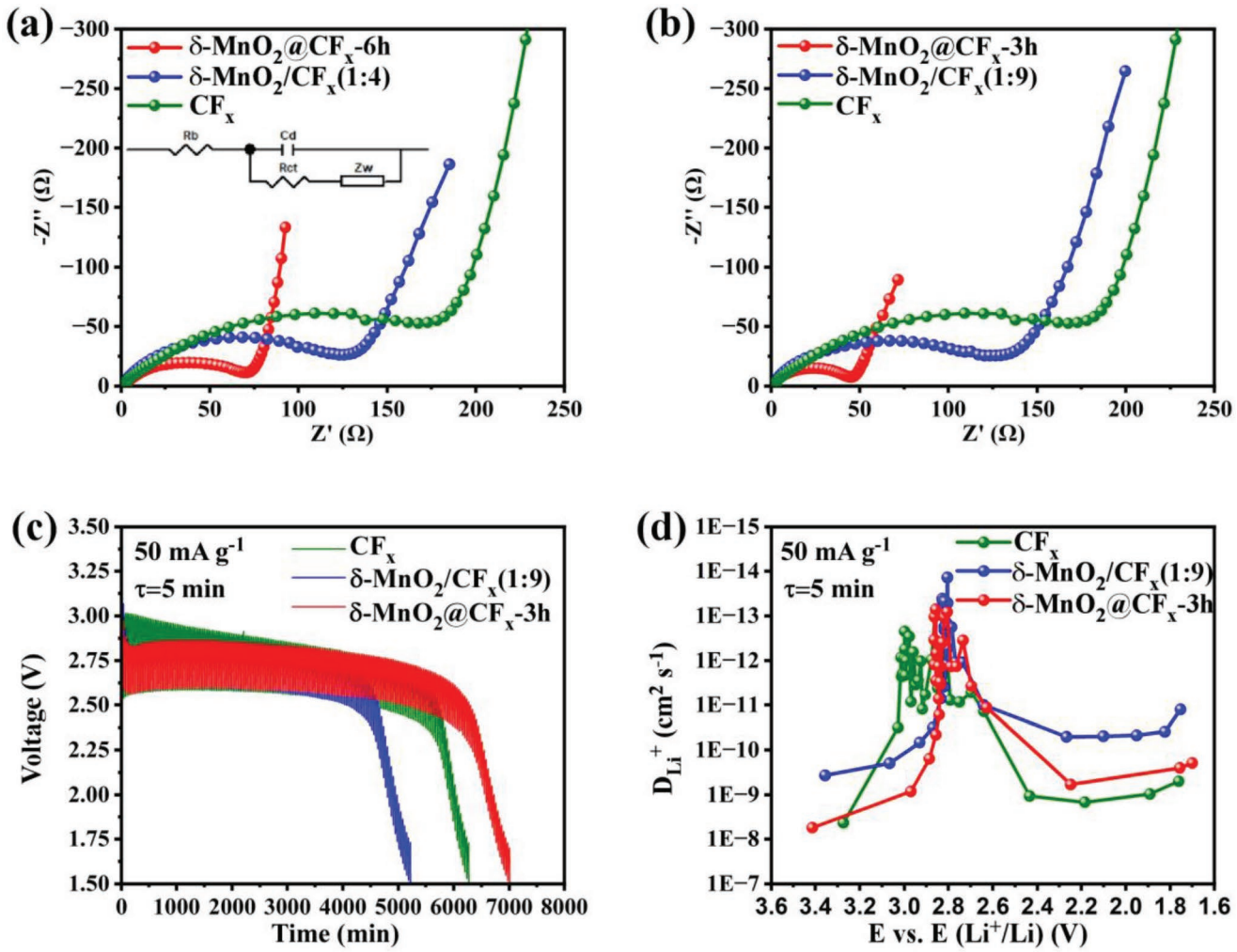

Figure 4. The electrochemical kinetics of CF_x, δ-MnO_2/CF_x and δ-MnO_2@CF_x cathodes. a) EIS spectra of CF_x, δ-MnO_2/CF_x(1:4) and δ-MnO_2@CF_x-6 h (inset: equivalent circuit model). b) EIS spectra of CF_x, δ-MnO_2/CF_x(1:9), and δ-MnO_2@CF_x-3 h. c) GITT test curves of CF_x, δ-MnO_2/CF_x(1:9), and δ-MnO_2@CF_x-3 h at current density of 50 mA g^{-1}. d) D_{Li}^+ calculated from the GITT data at 50 mA g^{-1}.

To further deeply understand the differences in electrochemical kinetics during discharge, galvanostatic intermittent titration technique (GITT) is applied to reveal the intrinsic reasons of the excellent rate capability of δ-MnO_2@CF_x-3 h by exploring the chemical diffusion coefficient of Li^+ (D_{Li}^+) (Figure 4c).[16] The coin cells fabricated by different cathodes are discharged at 50 mA g^{-1} for 5 min and rested for 30 min to ensure the voltage to relax to a steady-state value. The corresponding single-step GITT curves measured at 50 mA g^{-1} in 5–70 min are shown in Figure S6, Supporting Information. Specifically, Figure S7, Supporting Information, shows a voltage versus $\tau^{1/2}$ plot recorded for the CF_x, δ-MnO_2/CF_x(1:9), and δ-MnO_2@CF_x-3 h cathodes during the initial discharge period, respectively. The explored voltage and $\tau^{1/2}$ exhibit a significant linear relationship within the range of 4–25 s. Therefore, the simplified Fick''s second law is adopted to obtain the chemical diffusion coefficient of Li^+ in the CF_x, δ-MnO_2/CF_x(1:9), and δ-MnO_2@CF_x-3 h cathodes based on the following equation:

$$D_{Li^+} = \frac{4}{\pi}\left(I_0 \frac{V_m}{SFZ_i}\right)^2 \left(\frac{dE/dx}{dE/d\tau^{\frac{1}{2}}}\right)^2 \quad \left(\tau \ll L^2 / D_{Li^+}\right) \tag{1}$$

where I_0 is current; V_m and L are the molar volume and thickness of the electrode material, respectively; S is the contact area between the electrolyte and electrode; F is the Faraday constant; and Z_i is the number of charge transfers in the Li/CF_x battery during the discharge process. According to Equation (1), the functional relationship between D_{Li}^+ and the voltage in the discharge process is depicted in Figure 4d. It is observed that D_{Li}^+ in CF_x (10^{-8} cm^2 s^{-1}) is comparable to that in δ-MnO_2@CF_x-3 h initially. However, it decreases drastically to 10^{-12} cm^2 s^{-1} when the voltage drops to 3.0 V. In contrast, D_{Li}^+ in δ-MnO_2/CF_x(1:9) and δ-MnO_2@CF_x-3 h remains a high value and slowly drops to 10^{-11} cm^2 s^{-1} at 2.8 V as a result of the much faster reaction kinetics of the MnO_2 content during the initial discharge process,[38] which greatly inhibits the voltage delay effect of CF_x. Moreover, compared with δ-MnO_2/CF_x(1:9), the Li^+ diffusion coefficient in δ-MnO_2@CF_x-3 h is nearly an order of magnitude larger throughout the entire discharge process. This fast Li^+ diffusion in δ-MnO_2@CF_x-3 h can be ascribed to the uniformly distributed ultrathin MnO_2 flakes in close contact to the CF_x surface, which is able to ease the initial voltage delay without hindering the Li^+ diffusion pathway inside CF_x in the following discharge period. Nevertheless, as the reaction proceeds, the products of discharge (LiF) start to play a major role on leading the decrease of the D_{Li}^+ in electrodes and hindering the diffusion of Li^+.[10]

To further examine the discharge performance in large scale and explore the application potential, several pouch batteries of 1 Ah based on δ-MnO_2@CF_x-3 h cathodes (mass loading: 4 mg cm^{-2}) are fabricated as shown in **Figure 5**. It should be

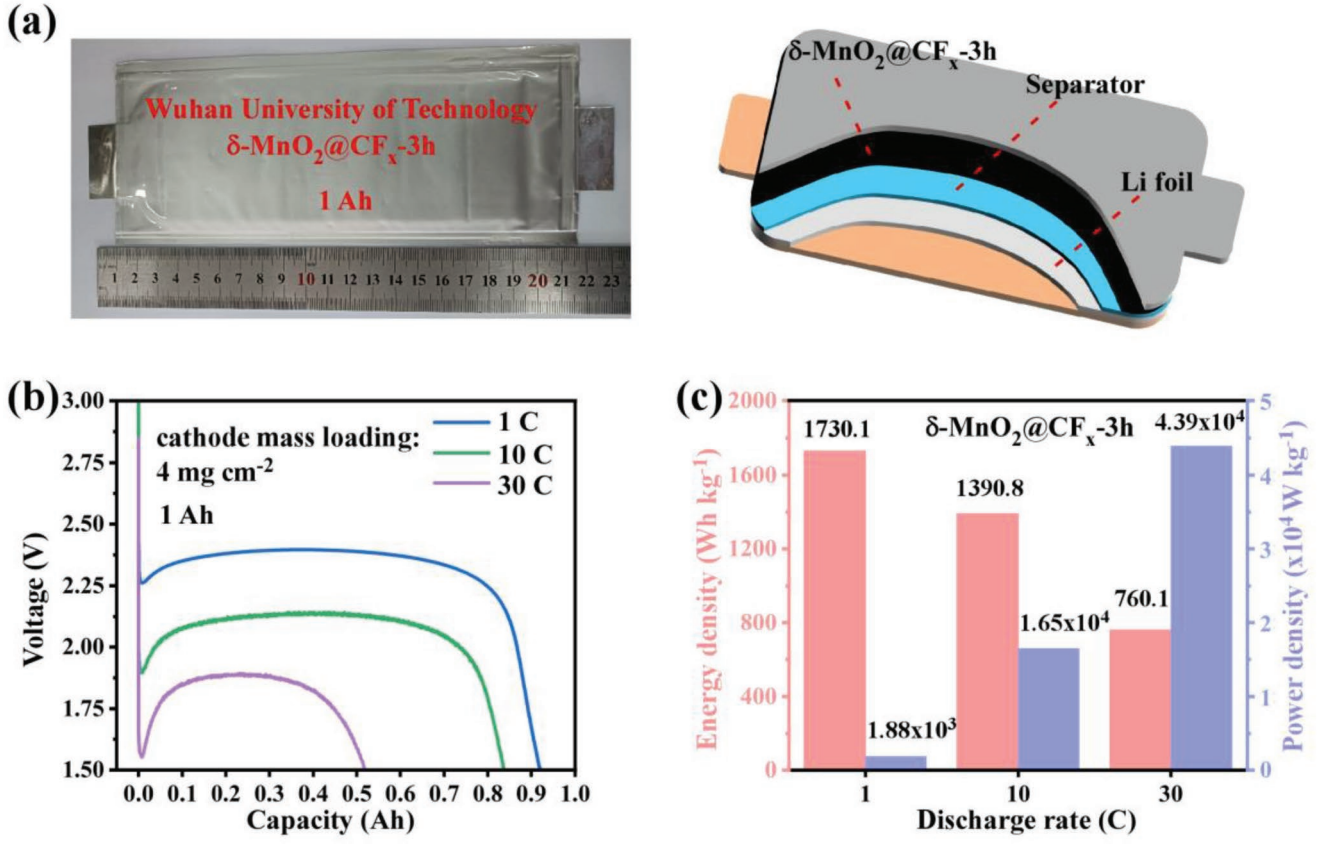

Figure 5. Electrochemical performance of the punch batteries with δ-MnO_2@CF_x-3 h. a) Photograph of the fabricated pouch battery and schematic diagram of a 3D pouch battery. b) Galvanostatic discharge curves of cathode mass loading of 4 mg cm^{-2} at 1 C, 10 C, and 30 C of δ-MnO_2@CF_x-3 h (1 Ah). c) Ragone plot of Li/δ-MnO_2@CF_x-3 h pouch battery at different discharge rates.

noted that the cell is of a high length-to-width ratio with battery tags placed at two sides (Figure 5a), which is suitable for high current discharge test. The open circuit voltage of the assembled Li/δ-MnO_2@CF_x-3 h pouch cell is around 3.45 V, and the GDCs are shown in Figure 5b. When discharged at 1 C, a capacity of 0.92 Ah with an average potential of ≈2.45 V can be obtained, and the corresponding specific capacity of δ-MnO_2@CF_x-3 h is 748.7 mAh g^{-1}. Furthermore, about 85% of the capacity can still be retained when the discharge current increases to 10 C. More impressively, the cell is able to deliver a capacity of about 0.52 Ah even when discharged at an ultrahigh rate of 30 C. The corresponding energy and power densities of the pouch battery based on the mass of active cathode materials are illustrated in Figure 5c. It can be seen that our pouch cells have achieved a high energy density of 1.73×10^3 Wh kg^{-1} at 1 C, and an ultrahigh power density of 4.39×10^4 W kg^{-1} with an energy density of 7.60×10^2 Wh kg^{-1} at 30 C. Compared with most of the previous works on Li/CF_x LPBs, these chemical modified δ-MnO_2@CF_x cathodes have great potentials in applications requiring both high energy density and power density such as aerospace.

To have a deeper understanding in the reaction mechanism, geometrical configurations and the corresponding binding energy calculated by density functional theory (DFT) of Li^+ bonded on CF_x, δ-MnO_2/CF_x and δ-MnO_2@CF_x are shown in **Figure 6**a. It can be seen that, compared with the bare CF_x and the physically mixed δ-MnO_2/CF_x, Li^+ prefers to bond with the chemical modified δ-MnO_2@CF_x. For the δ-MnO_2@CF_x composites, the chemical bonds formed between δ-MnO_2 and CF_x withdraw electrons from δ-MnO_2 as shown by the differential charge density analysis in Figure S8, Supporting Information, which leads to a much larger Li^+ binding energy of −1.78 eV on δ-MnO_2. Therefore, the chemically loaded δ-MnO_2 on CF_x is beneficial for the discharge reaction, which is consistent with the experimental results that δ-MnO_2@CF_x composites exhibit the best electrochemical performance among all the reference cathodes.

Based on the above experimental and theoretical results, we propose a three-stage discharge mechanism in Li/δ-MnO_2@CF_x systems as shown in Figure 6b: I) at the beginning of the discharge process, lithium ions start to react with δ-MnO_2 shell on the CF_x surface by intercalation due to the faster reaction kinetics, which is able to overcome the voltage delay of CF_x; II) in the second stage, the lithium ions start to react with the inside CF_x associated with the insertion of solvent molecules and form LiF, which propagates from edge to central sites of CF_x flakes; and III) in the third stage, the lithium ions continue to intercalate with the interfacial sites of CF_x flakes to form LiF along with the expansion of layer distance. Based on this edge-propagation discharge mechanism of CF_x,[39,40] it is

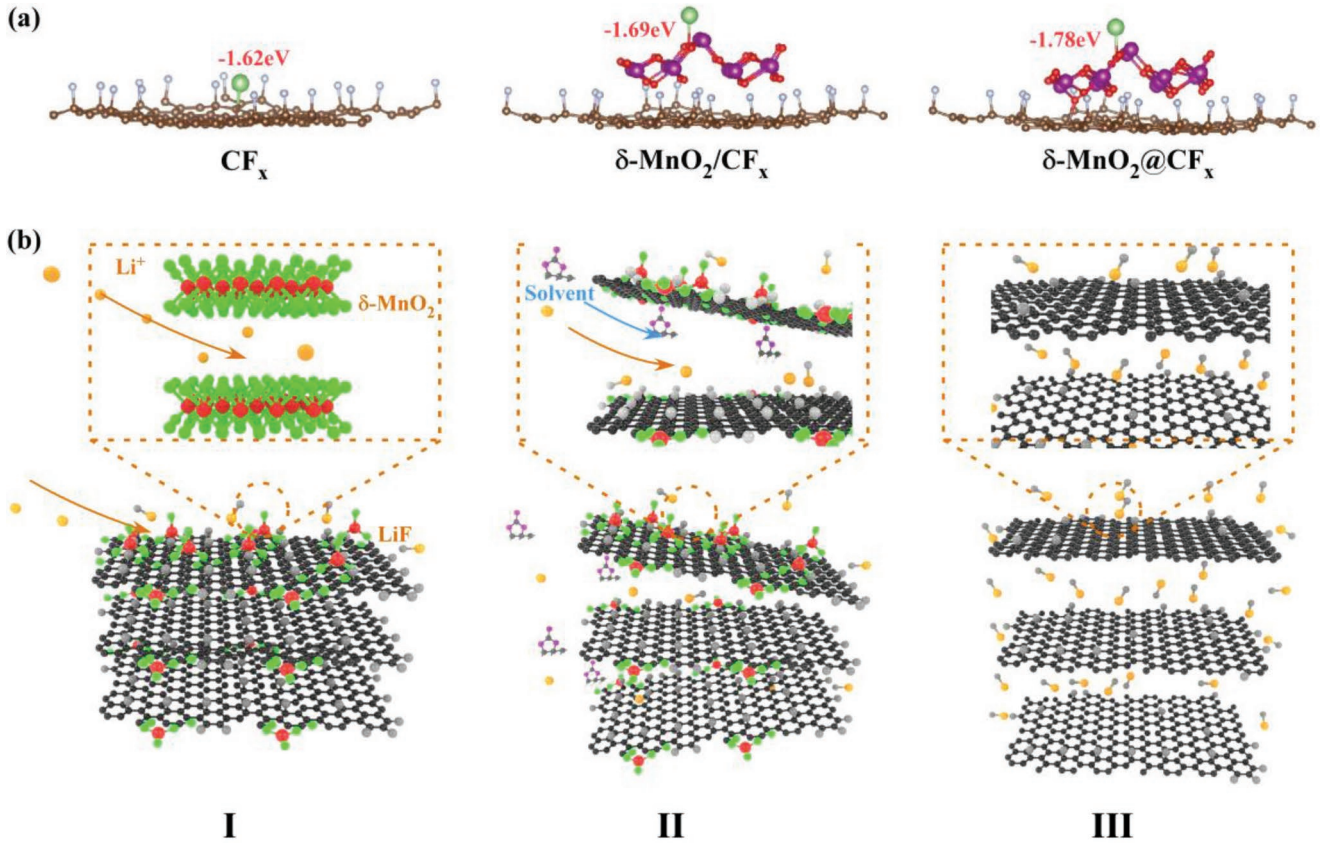

Figure 6. Theoretical calculations to illustrate the high-performance δ-MnO_2@CF_x cathodes. a) The geometrical configurations of the Li atom bonded to CF_x, δ-MnO_2/CF_x, and δ-MnO_2@CF_x cathodes. The lithium, carbon, oxygen, fluorine and manganese atoms are marked as dark, green, brown, red, gray and purple, respectively. b) The schematic mechanism of the Li/δ-MnO_2@CF_x system during discharge. The lithium, carbon, oxygen, fluorine and manganese atoms are marked as yellow, black, light green, gray and red, respectively.

suggested that a fast diffusion path of Li^+ is highly important for the improvement of electrochemical performance. Here, the ultrathin and precise chemical coating of δ-MnO_2 in δ-MnO_2@CF_x-3 h not only effectively reduce the amount of MnO_2 required for modification but also retain the original Li^+ diffusion path in CF_x, which results in an outstanding rate capability. Besides, the worse performance of δ-MnO_2@CF_x-6 h can be explained by a high Li^+ diffusion barrier through the thick δ-MnO_2 shell.

3. Conclusions

In summary, we demonstrate a chemical δ-MnO_2 coating method to modify CF_x through oxidation and hydrothermal reaction to develop δ-MnO_2@CF_x cathodes with excellent electrochemical properties. Morphology analysis reveals that tiny δ-MnO_2 flakes are uniformly and vertically distributed on the surface of CF_x in both δ-MnO_2@CF_x-3 h and δ-MnO_2@CF_x-6 h composites. The fabricated Li/δ-MnO_2@CF_x-3 h coin cells achieve extremely high-energy densities of 1.94×10^3 Wh kg^{-1} at 0.2 C and high power density of 5.49×10^4 W kg^{-1} at 40 C, while the value of Li^+ diffusion coefficient is around 10^{-10} cm^2 s^{-1}. Furthermore, Li/δ-MnO_2@CF_x-3 h pouch cells exhibit an energy density of 1.73×10^3 Wh kg^{-1} at 1 C and a power density of 4.39×10^4 W kg^{-1} at 30 C with a mass loading of 4 mg cm^{-2}. Based on atomic-level calculations via density functional theory (DFT), we theorize that the chemical coating played a vital role in providing a better chemical environment for the diffusion and insertion of Li^+. These findings of an accessible chemical modified Li/CF_x cathode with outstanding electrochemical performance shed new light on the design principles of CF_x-based cathodes, which also provides an innovative route for further development of LPBs with superior performance.

4. Experimental Section

Synthesis of δ-MnO_2@CF_x: 1 g CF_x (x = 0.6, Shandong Zhongshan Photoelectric Materials Co., Ltd.) were mixed with 75 mL of concentrated H_2SO_4 and 25 mL of concentrated HNO_3. After 1 h ultrasonication, the mixture was refluxed at 80 °C for 6 h with vigorously stirring to accomplish the oxidation process. After reaction, oxidized CF_x (O—CF_x) was filtered through a microporous membrane and washed with deionized (DI) water until the pH = 7. Finally, the oxidized product was obtained by vacuum drying at 80 °C for 12 h.

A typical synthesis process of the δ-MnO_2@CF_x composites is described as follows: first, 334 mg O—CF_x was dispersed in 84 mL DI water by ultrasonication for 2 h. Then, 0.25 g $KMnO_4$ was added into the above solution and the mixed solution was stirred by a magnetic bar for 2 h. After that, the mixed solution was transferred to a 100 mL Teflon-lined autoclave, which was put into an electric oven at 140 °C for certain time. After the hydrothermal treatment, the autoclave was naturally cooled to room temperature and the δ-MnO_2@CF_x composites were collected by filtration and washed with DI water. The composites were finally dried in an oven at 80 °C for 12 h for further characterization. To prepare the δ-MnO_2 powders, 0.25 g $KMnO_4$ and 0.2 mL H_2SO_4 (98 wt%) were dissolved in 84 mL DI water, and the precursor solution was then treated with a hydrothermal reaction in a 100 mL autoclave at 140 °C for 3 h.

Material Characterizations: Ex situ X-ray diffraction (XRD) measurement was performed using a Bruker AXS D2 Advance powder X-ray diffractometer with a detector using Cu Kα X-ray source. Scanning electron microscope (SEM) images were acquired by using a JEOL-7100F microscope. The high-resolution transmission electron microscopy (HRTEM) images, along with the high angular annular dark field image-scanning transmitted electron (HAADF-STEM) images and energy dispersive X-ray spectroscopy (EDX) tests were gained by utilizing microscope (Talos F200S). XPS analysis was carried out on Escalab 250Xi. Raman characterizations were measured with green laser (532 nm) using LABRAM HR Evolution Raman spectrometer. Fourier transform infrared spectroscopy (FT-IR) transmittance spectra was carried out by a Nicolet 6700 (Thermo Fisher Scientific Co., USA) IR spectrometer. Element content was detected by using an inductive coupled plasma emission spectrometer (ICP) on a PerkinElmer Optima 4300DV spectrometer.

Electrochemical Measurements: Active materials of δ-MnO_2, CF_x, δ-MnO_2/CF_x(1:4), δ-MnO_2/CF_x(1:9), δ-MnO_2@CF_x-6 h and the δ-MnO_2@CF_x-3 h were mixed with conductive carbon black (Acetylene black) and binder (PVDF), with weight ratios of 8:1:1, in an *N*-methyl-2-pyrrolidone solvent to form a uniform slurry, which was then coated on an aluminum foil to form the working electrode. After solvent evaporation, the electrodes were dried in vacuum at 70 °C for 24 h.[41] Electrochemical experiments were conducted based on the coin cell (CR2025-type), using a film punched into a 10 mm round disk as the cathode and Li metal as the anode. Celgard 2500 was used as separator. A solution of 1 M $LiClO_4$ dissolved in (PC:DME:DOL) (1:1:1 by volume) with 1 wt% $LiNO_3$ was selected as the electrolyte. The active material loading was 1.1–1.3 mg cm^{-2}. The cells were assembled in an argon-filled glove box. The pouch cells were assembled with double side coated cathodes (mass loading of 4 mg cm^{-2}), separators and Li metal anodes, which were sealed by aluminum-plastic films. Galvanostatic discharge and GITT tests were undertaken on a multi-channel battery testing system (LAND CT2001A) and the terminal voltage was 1.5 V. Electrochemical impedance spectroscopy (EIS) tests were carried out at open-circuit potential in the frequency range between 110 kHz and 0.03 Hz.

Supporting Information

Supporting Information is available from the Wiley Online Library or from the author.

Acknowledgements

L.L. and R.W. contributed equally to this work. The research was supported by the Hainan Provincial Joint Project of Sanya Yazhou Bay Science and Technology City (2021CXLH0007), and the National Natural Science Foundation of China (52127816, 61905183).

Conflict of Interest

The authors declare no conflict of interest.

Data Availability Statement

The data that support the findings of this study are available from the corresponding author upon reasonable request.

Keywords

chemical bonding, fluorinate carbon, lithium primary batteries, δ-MnO_2

Received: January 27, 2023
Revised: March 5, 2023
Published online:

[1] S. Su, J. Ma, L. Zhao, K. Lin, Q. Li, S. Lv, F. Kang, Y. B. He, *Carbon Energy* **2021**, *3*, 866.
[2] Y. Huang, *J. Alloys Compd.* **2022**, *1*, 323.
[3] Y. Dai, S. Cai, L. Wu, W. Yang, J. Xie, W. Wen, J.-C. Zheng, Y. Zhu, *J. Mater. Chem. A* **2014**, *2*, 20896.
[4] R. Yazami, A. Hamwi, K. Guérin, Y. Ozawa, M. Dubois, J. Giraudet, F. Masin, *Electrochem. Commun.* **2007**, *9*, 1850.
[5] R. Zhou, Y. Li, Y. Feng, C. Peng, W. Feng, *Compos. Commun.* **2020**, *21*, 100396.
[6] C. Peng, Y. Li, F. Yao, H. Fu, R. Zhou, Y. Feng, W. Feng, *Carbon* **2019**, *153*, 783.
[7] M. Dubois, K. Guérin, W. Zhang, Y. Ahmad, A. Hamwi, Z. Fawal, H. Kharbache, F. Masin, *Electrochim. Acta* **2012**, *59*, 485.
[8] P. Meduri, H. H. Chen, X. L. Chen, J. Xiao, M. E. Gross, T. J. Carlson, J. G. Zhang, Z. D. Deng, *Electrochem. Commun.* **2011**, *13*, 1344.
[9] H. Groult, C. M. Julien, A. Bahloul, S. Leclerc, E. Briot, A. Mauger, *Electrochem. Commun.* **2011**, *13*, 1074.
[10] L. Kong, Y. Li, C. Peng, L. Sun, K. Wang, Y. Liu, W. Feng, *Nano Energy* **2022**, *104*, 107905.
[11] Y. L. Zhu, L. J. Zhang, H. J. Zhao, Y. Fu, *J. Mater. Chem. A* **2017**, *5*, 796.
[12] Z. Luo, X. Wang, D. Chen, Q. Chang, S. Xie, Z. Ma, W. Lei, J. Pan, Y. Pan, J. Huang, *ACS Appl. Mater. Interfaces* **2021**, *13*, 18809.
[13] Q. Zhang, S. D. Astorg, P. Xiao, X. Zhang, L. Lu, *J. Power Sources* **2010**, *195*, 2914.
[14] S. S. Zhang, D. Foster, J. Read, *J. Power Sources* **2009**, *188*, 601.
[15] G. Chen, H. Zhou, S. Zhang, Z. Zhang, T. Feng, Z. Xu, M. Wu, *ACS Appl. Energy Mater.* **2021**, *4*, 8615.
[16] Y. Li, W. Feng, *J. Power Sources* **2015**, *274*, 1292.
[17] Z. Luo, J. Wan, W. Lei, Y. Zhao, Y. Pan, Z. Ma, *Mater. Technol.* **2019**, *35*, 836.
[18] X. Wang, Y. Dai, J. Gao, J. Huang, B. Li, C. Fan, J. Yang, X. Liu, *ACS Appl. Mater. Interfaces* **2013**, *5*, 8294.
[19] L. Cheng, S. Jandhyala, G. Mordi, A. T. Lucero, J. Huang, A. Azcatl, R. Addou, R. M. Wallace, L. Colombo, J. Kim, *ACS Appl. Mater. Interfaces* **2016**, *8*, 5002.
[20] C. B. Sun, Y. Y. Feng, Y. Li, C. Q. Qin, Q. Q. Zhang, W. Feng, *Nanoscale* **2014**, *6*, 2634.
[21] G. L. Wang, Y. L. Wang, B. Y. Guan, J. M. Liu, Y. Zhang, X. W. Shi, C. Tang, G. H. Li, Y. B. Li, X. Wang, L. Li, *Small* **2021**, *17*, 2104557.
[22] Q. Chen, J. L. Jin, Z. K. Kou, C. Liao, Z. Liu, L. Zhou, J. Wang, L. Q. Mai, *Small* **2020**, *16*, 2000091.
[23] R. Fang, Q. Feng, H. Huang, J. Ji, M. He, Y. Zhan, B. Liu, D. Y. C. Leung, *Catal. Today* **2019**, *327*, 154.
[24] Q. Chu, X. Wang, X. Zhang, Q. Li, X. Liu, *Inorg. Chem.* **2011**, *50*, 2049.
[25] Y. Y. Li, X. Z. Wu, C. Liu, S. Wang, P. F. Zhou, T. Zhou, Z. C. Miao, W. Xing, S. P. Zhuo, J. Zhou, *J. Mater. Chem. A* **2019**, *7*, 7128.
[26] J. Wang, J.-G. Wang, H. Liu, Z. You, Z. Li, F. Kang, B. Wei, *Adv. Funct. Mater.* **2021**, *31*, 2007397.
[27] J.-G. Wang, F. Kang, B. Wei, *Prog. Mater. Sci.* **2015**, *74*, 51.
[28] H. Jia, Y. Cai, J. Lin, H. Liang, J. Qi, J. Cao, J. Feng, W. Fei, *Adv. Sci.* **2018**, *5*, 1700887.
[29] J. Tan, F. A. Soto, J. Noh, P. Wu, D. R. Yadav, K. Xie, P. B. Balbuena, C. Yu, *J. Mater. Chem. A* **2021**, *9*, 9291.
[30] K. Yang, Z. Shan, X. Liu, S. Wang, *Mater. Lett.* **2022**, *309*, 131421.
[31] J. Hou, F. Cao, H. Xu, J. A. Fu, R. Ali, Y. F. Liu, X. Jian, *Appl. Surf. Sci.* **2022**, *596*, 153570.
[32] T. A. Saleh, S. Agarwal, V. K. Gupta, *Appl. Catal., B* **2011**, *106*, 46.
[33] H. Xia, Y. Wang, J. Y. Lin, L. Lu, *Nanoscale Res. Lett.* **2012**, *7*, 33.
[34] P. Xiong, R. Ma, N. Sakai, X. Bai, S. Li, T. Sasaki, *ACS Appl. Mater. Interfaces* **2017**, *9*, 6282.
[35] W. M. Dose, S. W. Donne, *Electrochim. Acta* **2013**, *105*, 305.
[36] Y. Dai, Y. Fang, S. Cai, L. Wu, W. Yang, H. Yan, J. Xie, J.-C. Zheng, E. Takeuchi, Y. Zhu, *J. Electrochem. Soc.* **2016**, *164*, A1.
[37] G. H. An, H. Kim, H. J. Ahn, *ACS Appl. Mater. Interfaces* **2018**, *10*, 6235.
[38] Q. Xie, G. Cheng, T. Xue, L. Huang, S. Chen, Y. Sun, M. Sun, H. Wang, L. Yu, *Mater. Today Energy* **2022**, *24*, 100934.
[39] K. Leung, N. B. Schorr, M. Mayer, T. N. Lambert, Y. S. Meng, K. L. Harrison, *Chem. Mater.* **2021**, *33*, 1760.
[40] B. Sayahpour, H. Hirsh, S. Bai, N. B. Schorr, T. N. Lambert, M. Mayer, W. Bao, D. Cheng, M. Zhang, K. Leung, K. L. Harrison, W. Li, Y. S. Meng, *Adv. Energy Mater.* **2021**, *12*, 2103196.
[41] Y. Xia, J. Li, Z. Xiao, X. Zhou, J. Zhang, H. Huang, Y. Gan, X. He, W. Zhang, *ACS Appl. Mater. Interfaces* **2022**, *14*, 33361.
[42] W. Yang, Y. Dai, S. Cai, Y. Zheng, W. Wen, K. Wang, Y. Feng, J. Xie, *J. Power Sources* **2014**, *255*, 37.
[43] Q. Li, W. Xue, X. Sun, X. Yu, H. Li, L. Chen, *Energy Storage Materials* **2021**, *38*, 482.